







# A Near-Infrared Enhanced Field-Line Crowding Based CMOS-Integrated Avalanche Photodiode

Seyed Saman Kohneh Poushi , Christoph Gasser , Bernhard Goll , *Member, IEEE*,  
Michael Hofbauer , *Member, IEEE*, Kerstin Schneider-Hornstein ,  
and Horst Zimmermann , *Senior Member, IEEE*

**Abstract**—This paper presents a CMOS-integrated linear-mode avalanche photodiode based on electric field-line crowding (EFLC-APD) to form an effective multiplication zone and a wide absorption zone. The EFLC-APD possesses a hemispherical avalanching electric field at the n-well/p-epi junction formed due to the curvature of the half-sphere cathode. A lower electric field extends radially across the entire volume of the EFLC-APD towards the substrate and towards the surface anode. Because of such a distribution of the electric field, electrons photogenerated within the whole volume drift towards the cathode. Therefore, the EFLC-APD provides a large sensitive-area to total-area ratio while offering high responsivity and bandwidth for red and near-infrared light due to its thick absorption zone and drift-based carrier transport. It is shown that the electric field distribution can be modified by the design parameters such as cathode radius and diode size in addition to doping profiles. The EFLC-APD achieves a responsivity-bandwidth (R-BW) product of  $49.5 \frac{\text{A}}{\text{W}} \cdot \text{GHz}$ , corresponding to the responsivity and bandwidth of  $33 \text{ A/W}$  and  $1.5 \text{ GHz}$ , respectively, at the wavelength of  $850 \text{ nm}$ . In addition, a maximum responsivity of  $3.05 \times 10^3 \text{ A/W}$  at  $2 \text{ nW}$  optical power is achieved for the red and near-infrared spectral range. Noise characterization resulted in an excess noise factor  $F = 6$  measured at an avalanche gain of  $56.7$ . Due to the high sensitive-area to total-area ratio, high responsivity, large bandwidth, and CMOS compatibility, this APD is a promising optical detector for many applications.

**Index Terms**—CMOS integrated avalanche photodiode, linear-mode avalanche photodiode, field-line crowding, spherical avalanching field, near-infrared light.

## I. INTRODUCTION

THE ability to detect low-power optical signals is one of the main challenges in the field of applied optical sensors. The internal amplification makes linear-mode avalanche photodiodes (APDs) interesting optical detectors for many optical systems that require low light detection such as optical wireless communication (OWC) [1], [2], [3], [4], light detection and ranging applications (LIDAR) [5], [6], and imaging sensors [7], [8]. The use of APDs integrated with electronic circuitry by complementary metal-oxide semiconductor (CMOS) technology has become attractive in optical systems.

Manuscript received 2 May 2023; revised 22 May 2023; accepted 23 May 2023. Date of publication 26 May 2023; date of current version 2 June 2023. This work was supported by the Austrian Science Fund FWF, under Grant P34649. (Corresponding author: Seyed Saman Kohneh Poushi.)

The authors are with the Institute of Electrodynamics, Microwave, Circuit Engineering, Vienna University of Technology, 1040 Vienna, Austria (e-mail: saman.kohneh@tuwien.ac.at).

Digital Object Identifier 10.1109/JPHOT.2023.3280251

Si CMOS integrated APDs typically use a planar  $n^+/p$ -well or a  $p^+/n$ -well junction to provide a space-charge region as detection zone and a high field region for multiplying the photo-generated carriers. The thickness of the detection region in these APDs is in the order of hundreds of nanometres [9], [10], [11], [12], [13], [14]. These structures achieve good results in terms of bandwidth because of a thin depleted absorption region. Ref. [13] reported a bandwidth of  $8.4 \text{ GHz}$  for an APD based on a  $p$ -well/deep  $n$ -well structure, and Ref. [14] achieved a bandwidth of  $12 \text{ GHz}$  for a spatially modulated APD. However, these APDs suffer from low responsivity due to the non-contribution of carriers generated under the thin absorption region to the output current. The maximum responsivities of the APDs reported in [13] and [14] for a wavelength of  $850 \text{ nm}$  are respectively  $0.56 \text{ A/W}$  and  $0.03 \text{ A/W}$ .

A so-called reach-through design concept was proposed to widen the absorption region, and thereby improve the responsivity [15], [16], [17], [18]. These thick APDs provide a space-charge region with a thickness in the range of  $10 \mu\text{m}$ . A maximum responsivity of  $2.7 \times 10^4 \text{ A/W}$  for  $5\text{-nW}$  optical power at  $670 \text{ nm}$  was reported in Ref. [16]. The main drawback of such structures is their limited bandwidth due to the higher carrier drift time in a thick absorption zone. The maximum bandwidth reported in Ref. [16] is  $850 \text{ MHz}$ . Ref. [19] used a modulation doping technique for speed optimization to enhance the bandwidth to  $1.25 \text{ GHz}$  while maintaining the high responsivity but at a high reverse voltage of  $115 \text{ V}$ , where the diode could not longer be well isolated from the circuits on the chip.

Besides, in these planar structures, the photo-sensitive area is limited by the area of the  $p/n$  junction. In fact, carriers generated in the peripheral volume have a low probability of moving through the multiplication region and of leading to avalanche events, which leads to a limited sensitive-area to total-area ratio. In addition, they require a (virtual) guard ring to prevent premature edge breakdown due to a locally concentrated electric field at the edge of the junction, which further degrades the ratio of sensitive-area to total-area [20], [21], [22], [23]. This sensitive-area limitation is more substantial when the APD is downsized, in which the peripheral region is comparable to the dimensions of the photo-sensitive area [24].

Ref. [25] proposed a current-assisted avalanche photodiode that can collect charges generated in the peripheral volume. Two electrodes at the surface with different potentials are employed to form a drifting electric field for guiding the electrons

photogenerated in the peripheral volume towards the central multiplication region. This APD exhibits a high ratio of sensitive-area to total-area, however, achieves a maximum bandwidth of 275 MHz and 13 A/W responsivity at a wavelength of 830 nm.

Refs. [26], [27], [28] employed a charge-focusing concept to collect peripheral charge carriers in designing of single-photon avalanche photodiode (SPAD). In [26], [27], a customized fabrication process was utilized, involving a shallow n-type implant between the cathode and anode. This modification aimed to redistribute the electric field just below the silicon/silicon dioxide interface at the surface of the device, specifically to reduce the dark count rate. Ref. [29] presented a silicon photomultiplier (SiPM) that utilizes a SPAD based on the field-line crowding effect. However, transistors cannot be fabricated in the special SiPM detector process.

Recently, we presented a new Si CMOS APD based on the field-line crowding concept, which can be fabricated in a standard CMOS process without any process modification [30]. The EFLC-APD possesses a small hemispherical multiplication region around the n-well/p-epi junction and a thick depleted volume in the p-epitaxial layer with a lower electric field to guide charge carriers from the whole diode volume towards the multiplication region. This structure provides a maximum bandwidth of 1.6 GHz with a responsivity of  $R = 32$  A/W at a wavelength of 675 nm while having a high sensitive-area to total-area ratio. The superiority of the EFLC-APD at down-scaling with maintaining the overall sensitivity and providing a large sensitive-area make it a very promising candidate to be used in array sensors.

In this article, we study the performance of the EFLC-APD for near-infrared light and improve the frequency response using electric field modification. TCAD simulation is used to study the effect of design parameters on the electric field distribution across the structure and consequently on the performance. The distributed field throughout the structure results in high bandwidth and responsivity due to providing a thick absorption region and drift-based carrier transport.

## II. APD STRUCTURE

Fig. 1 shows a schematic 3-D drawing with the doping regions (a) and the top view (b) of the EFLC-APD fabricated in 0.18  $\mu\text{m}$  high-voltage CMOS technology. The cathode of this APD consists of a hemispherical highly-doped  $n^+$  region with a radius of 0.37  $\mu\text{m}$  embedded in a half-sphere n-well region with a radius of  $r_w$ . The round implant regions are made by using polygons with very short side lengths as well as 0, 90 and 135° angles that form the circle. The cathode is connected to the cathode pad with a track in metal layer 3 with a width of 2  $\mu\text{m}$  as shown in Fig. 1(b). It should be noticed that the metal line used to connect the cathode to the cathode pad passes through the isolation layer on top of the active area. Since metal is an opaque material, therefore this area is practically no longer contributing to the absorption region, which degrades the sensitive-area to total-area ratio. The ratio of the area under the metal to the entire active area volume would be around 3.3% given by  $\frac{2 \times 19}{19^2 \times \pi}$ . The cathode is surrounded by a  $p^+$  and p-well ring (inner radius =

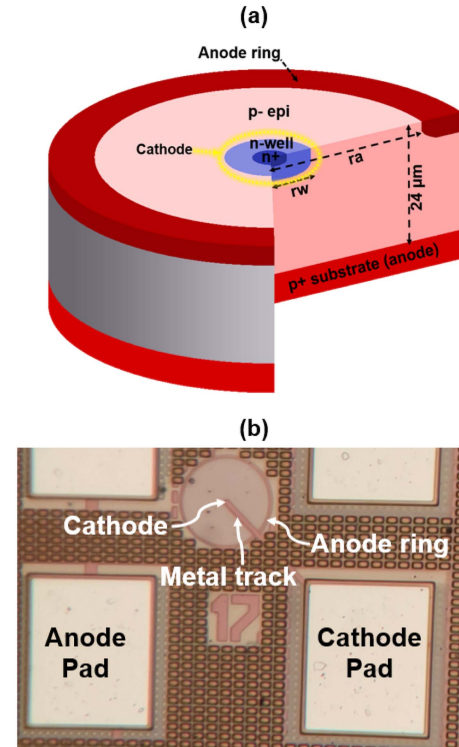


Fig. 1. (a) 3D schematic drawing (not to scale) and (b) top view of the fabricated EFLC-APD. The APD is covered by a standard isolation and passivation stack (not shown).

$r_a$ ) used as an anode ring. These regions are formed at the surface of a lightly p-doped ( $\sim 1.5 \times 10^{13} \text{ cm}^{-3}$ ) epitaxial layer (p-epi) with a thickness of  $\sim 24 \mu\text{m}$ . The  $p^+$  substrate is also used as a substrate anode. On the top of the silicon, there is a standard isolation and passivation stack to protect the fabricated device from environmental influences.

When the EFLC-APD is reversely biased, a hemispherical space-charge region forms around the cathode, which extends towards the substrate and the anode ring as the operating voltage increases. The electric field distribution of the space-charge region can be obtained from Gauss's law under two assumptions: the dimension of the highly doped cathode is much smaller than the whole diode volume, and it forms an abrupt transition into the intrinsic layer. Accordingly, the one-dimensional electric field in spherical coordinates is:

$$E(d) \approx \frac{(V_r + V_{bi})r_w}{d^2}, \quad (1)$$

where  $V_{bi}$  is the built-in voltage,  $V_r$  is the operation voltage, and  $r_w$  is the cathode's radius. According to 1, in reverse direction, a spherical high electric field region forms at the n-well/p-epi junction, and extends towards the substrate and towards the anode ring but decays by moving radially away from the center at a rate of  $d^{-2}$ .

## III. TCAD SIMULATION

In order to study the electric field distribution inside the structure, TCAD simulations were performed using Silvaco's

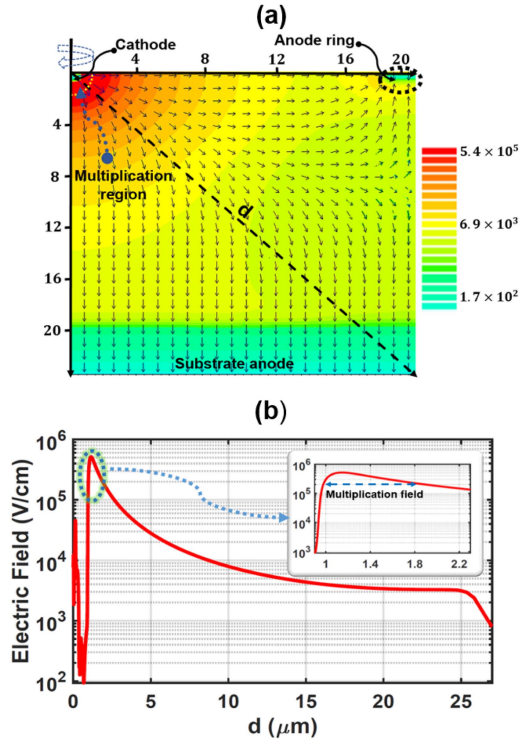


Fig. 2. (a) 2D plot of the electric field distribution across the EFLC-APD ( $rw = 0.6 \mu\text{m}$ ,  $ra = 19 \mu\text{m}$ ) at  $V_r = 69 \text{ V}$ , corresponding to a gain ( $M$ ) of 80. The breakdown voltage is  $70.7 \text{ V}$ . Vector arrows represent the local electric field direction. (b) Radial section of the electric field along the vector  $d$  in the structure.

ATLAS [31]. Fig. 2(a) shows a 2D plot of the electric field within the EFLC-APD at an operating voltage of  $69 \text{ V}$ . It can be seen that a high field ( $E \gtrsim 2 \times 10^5 \text{ V/cm}$ ) region with a width of  $\sim 0.9 \mu\text{m}$  forms around the cathode, which is called multiplication region. This high field provides enough kinetic energy to create avalanche events due to impact ionization.

The electric field decreases by moving radially away from the center towards the substrate and towards the anode ring, but it is still in the range of thousands of  $\text{V/cm}$  at  $25 \mu\text{m}$  away from the origin of coordinates as shown in Fig. 2(b). This electric field accelerates the photogenerated electrons in the direction opposite to the vector arrows and guides them towards the multiplication region. Due to such a distributed electric field throughout the structure, absorbed photons in the entire epitaxial layer have a very high chance to cause impact ionization by electrons drifting to the cathode, which results in a high sensitive-area to total-area ratio. Consequently, the large thickness of the detection zone provides high responsivity for long wavelengths, and the drift-based carrier transport mechanism enhances the detector's speed performance.

The distribution of the electric field changes with the radius of the n-well ( $rw$ ) while the doping (implantation energy and dose as well as thermal budget) remains constant. Fig. 3(a) illustrates the electric field distribution for different n-well radii at a constant doping concentration. It can be seen that as the radius of the n-well decreases, the strength of the electric field

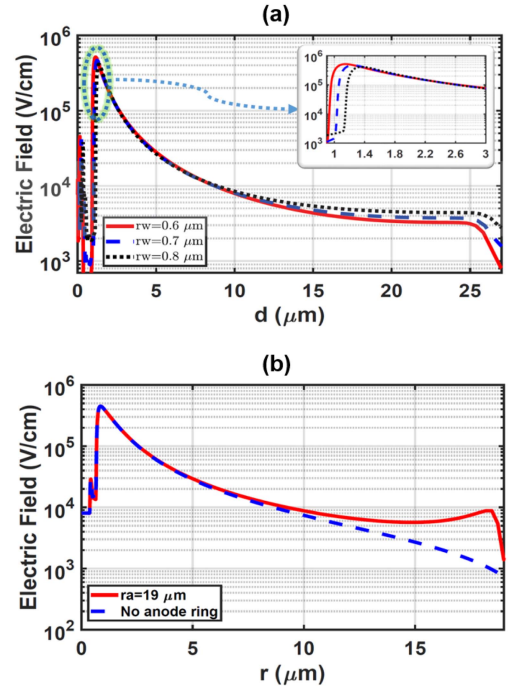


Fig. 3. (a) Radial cross-section of the electric field in the EFLC-APD with  $ra = 19 \mu\text{m}$  for different n-well radii. (b) Lateral cross-section of the electric field at the silicon surface of the EFLC-APD with  $rw = 0.6 \mu\text{m}$ . Simulations are done at an operating voltage of  $69 \text{ V}$ ,  $73.5 \text{ V}$ , and  $80 \text{ V}$  for  $rw = 0.6 \mu\text{m}$ ,  $rw = 0.7 \mu\text{m}$ , and  $rw = 0.8 \mu\text{m}$ , respectively, which all correspond to a gain of 80.

increases in the multiplication region (see the inset in Fig. 3(a)) and decreases in the detection zone (see Fig. 3(a) especially for  $d = 10$  to  $25 \mu\text{m}$ ). This is due to the fact that by decreasing the n-well radius, the curvature of the n-well region becomes sharper, leading to a higher electric field at the n-well/p-epi junction. Therefore, it should be considered that in order to provide enough electric field in the detection zone, EFLC-APDs with a larger size need an n-well with a larger radius.

Furthermore, the use of the anode ring redistributes the electric field in the lateral direction. Fig. 3(b) shows the lateral cross-section of the electric field at the silicon surface of the EFLC-APD structures with and without the anode ring. It can be seen that in the EFLC-APD with the anode ring, the electric field increases around the anode and then sharply drops. However, in the case there is no anode ring, the electric field is weaker, but could extend wider in the lateral direction. Here, the radius of the anode ring of  $ra = 19 \mu\text{m}$  is about the same as the vertical thickness of the effective intrinsic region (note: the  $p^+$  substrate diffused a few  $\mu\text{m}$  into the grown  $24 \mu\text{m}$  epi layer during the epitaxy and during the CMOS process) which is perfectly fitted to get the spherical shape.

It should be noted that changes in electric field distribution lead to different frequency responses of the diode. In fact, the frequency response is determined by the transit time of photogenerated electrons to reach the cathode. The transit time depends on the carrier drift distance and the drift velocity, which is proportional to the local electric field strength. The electric field gradually decreases (below the threshold required

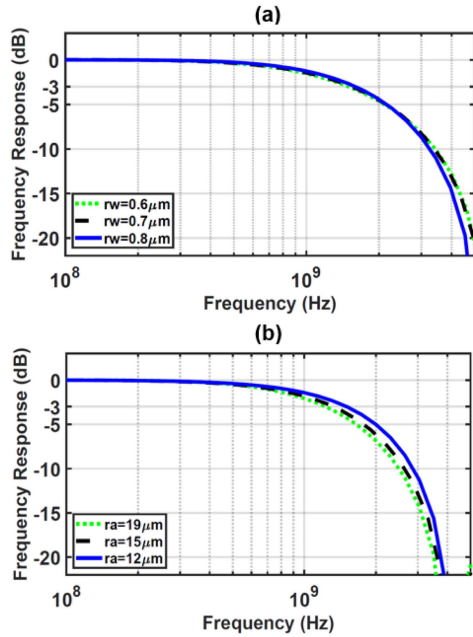


Fig. 4. Normalized frequency responses at  $\lambda = 850$  nm for different (a) n-well radii and (b) diode sizes, extracted from TCAD simulations. Simulations are done at an operating voltage of (a) 69 V, 73.5 V, 80 V for  $rw = 0.6$   $\mu\text{m}$ ,  $rw = 0.7$   $\mu\text{m}$ ,  $rw = 0.8$   $\mu\text{m}$ , respectively, and (b) 60 V, 64 V, 69 V for  $ra = 12$   $\mu\text{m}$ ,  $ra = 15$   $\mu\text{m}$ , and  $ra = 19$   $\mu\text{m}$ , respectively. Note: these voltage values were selected to achieve a gain of 80 for each respective configuration.

for saturated drift velocity) by moving radially away from the center. Accordingly, the bandwidth is limited by the drift time of photogenerated electrons absorbed in the thick absorption region far away from the center in the diagonal direction.

In order to study the influence of the electric field distribution on the frequency response, Fig. 4 represents the frequency response for the different n-well radii ( $rw$ ) and different diode sizes ( $ra$ ). The bandwidths achieved by the EFLC-APDs with a  $ra$  of 12 and different  $rw$  values of 0.6, 0.7, and 0.8  $\mu\text{m}$  are 1.5, 1.54, and 1.59 GHz, respectively. The slight increase in bandwidth observed for the diodes with a larger n-well radius can be attributed to the slightly higher electric field in the detection zone, enabling faster carrier transit. According to Fig. 4(b), the speed can be improved by reducing the size of the diode, but at the cost of reducing the active area. The EFLC-APDs with an  $rw$  of 0.6  $\mu\text{m}$  and different sizes of 19, 15, and 12  $\mu\text{m}$  achieve bandwidths of 1.23, 1.35, and 1.5 GHz, respectively. This is because as the size of the diode decreases, the electric field strength distributed across the detection region increases and in addition, the radial carrier drift distance shortens. Furthermore, the effect of these parameters on the breakdown voltage is discussed in the following. Accordingly, such parameters should be optimized based on the requirements of the intended application.

#### IV. MEASUREMENT RESULTS

Here, some key performance characteristics such as breakdown voltage, gain ( $M$ ), responsivity ( $R$ ), bandwidth ( $BW$ ), and noise of the EFLC-APD are discussed. We have performed the measurements on wafer using a wafer prober at a constant

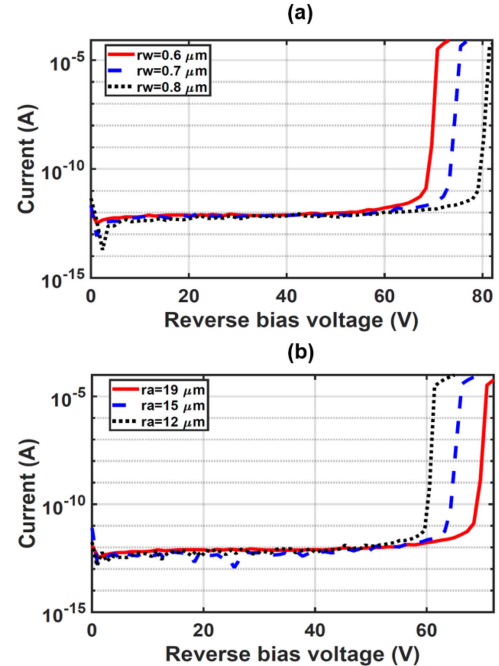


Fig. 5. Dark reverse characteristics for (a) different cathode radii with  $ra = 19$   $\mu\text{m}$ , (b) different diode size with  $rw = 0.6$   $\mu\text{m}$ .

temperature of 25  $^{\circ}\text{C}$  with probe heads. A Keysight B2987A electrometer was used to supply the voltage and measure the current.

##### A. Breakdown Voltage

As it was explained before, the distribution of the electric field within the structure changes as the radius of the n-well varies that leads to different breakdown voltages. Fig. 5(a) illustrates the dark characteristics of the EFLC-APDs with different n-well radii. The EFLC-APD with  $rw = 0.6$   $\mu\text{m}$  exhibits a breakdown voltage of 70.7 V, where the dark current reaches 1  $\mu\text{A}$ . It is important to note that the presented APD is designed to operate at substrate potentials of about  $-69$  V. However, the high-voltage (HV) CMOS process used for fabrication offers different wells to isolate the MOS transistors, enabling substrate potentials as low as  $-100$  V. As a result, the high operating voltage of the EFLC-APD does not hinder the integration of such APD with readout circuits on the same silicon chip. It seems that the current is saturated at a current level of  $\sim 50$   $\mu\text{A}$ . This is because of high contact and series resistance. As the cathode is very small, there is only one contact via in the cathode, which makes a high contact resistance. Furthermore, we applied the biasing voltage only on the anode ring, not at the reverse substrate contact as we used a diced chip mounted on an insulating holder for the measurement. Therefore, there is a series resistance between the anode and cathode in the present device. It is, however, possible to reduce the series resistance by using a large-area p+/p-well anode contact at the silicon surface.

It can be seen that a larger n-well radius results in a higher breakdown voltage. This is because the electric field strength in the multiplication region (i.e., around the n-well) lowers with

increasing the n-well radius, and accordingly a higher operating voltage is required to provide the same avalanche gain. As a result, the operating voltage can be lowered by reducing the n-well radius. However, shrinking the n-well region is limited by a technology-associated design rule. The advanced, smaller-node technologies offer smaller n-well radii. In addition, they provide higher doping concentrations. Therefore, it is possible to design EFLC-APDs with lower breakdown voltage in advanced smaller node CMOS technologies. Of course, less lateral spread of the space-charge region and a reduction of the drift velocity will be the consequence. A high bandwidth, then, requires a reduction of the light-sensitive area (radius) or multi-dot structures with many cathode dots.

In addition, the breakdown voltage is influenced by the radius of the anode ring as the lateral electric field distribution inside the structure varies for different anode ring radii as mentioned in Section II. Fig. 5(b) shows the dark characteristics of the EFLC-APDs with different anode ring radii. It can be seen that by decreasing the anode ring radius, the breakdown voltage lowers. In fact, by reducing the anode radius from  $19 \mu\text{m}$  to  $12 \mu\text{m}$ , the breakdown voltage changes from  $70.7 \text{ V}$  to  $60.5 \text{ V}$ . This is due to the fact that by decreasing the diode size, the electric field is distributed over a smaller volume, leading to a higher intensity in the multiplication and detection zone.

### B. Gain and Responsivity

The photodetection characterization of the EFLC-APD has been done for red ( $\lambda = 675 \text{ nm}$ ) and near-infrared light ( $\lambda = 850 \text{ nm}$ ). A multi-mode fiber with a lensed tip is used to provide a spotlight with a radius of  $12.5 \mu\text{m}$ , which is smaller than the radius of the active area so that the total light was irradiated into the active area and all incident photons had the chance to be detected.

Fig. 6(a) shows the responsivity as a function of the reverse bias voltage at a low optical power (op) of  $2 \text{ nW}$ , obtained from the photocurrent characteristics, where the dark current has been subtracted. It can be seen that this APD shows almost the same responsivity for  $\lambda = 850 \text{ nm}$  as it was obtained for  $\lambda = 675 \text{ nm}$  in [30]. An unamplified responsivity ( $M = 1$ ) of  $0.42 \text{ A/W}$  for  $850 \text{ nm}$  at  $V_0 = 1 \text{ V}$  is achieved, which corresponds to the quantum efficiency of  $61.4\%$ . It should be mentioned that not every incident photon is transmitted into the silicon due to the non-zero surface reflectivity of the Si/isolation and passivation stack interface, which degrades the responsivity. Nevertheless, a maximum responsivity of  $3.05 \times 10^3 \text{ A/W}$  at  $op = 2 \text{ nW}$  and  $V = 70.5 \text{ V}$  ( $rw = 0.6 \mu\text{m}$ ,  $ra = 19 \mu\text{m}$ ), which corresponds to a gain of  $7.26 \times 10^3$ , is achieved for both wavelengths (see the spectral response in Fig. 6).

Fig. 6(b) shows the spectral responsivity of the EFLC-APD with  $rw = 0.6 \mu\text{m}$  and  $ra = 19 \mu\text{m}$  at  $op = 2 \text{ nW}$  for different gains. We used a Digikröm CM110 monochromator that swept the wavelength from  $400 \text{ nm}$  to  $900 \text{ nm}$  by steps of  $1 \text{ nm}$ , coupled with an optical attenuator to set the optical power at a constant value of  $2 \text{ nW}$ . The dependence of the photodiode responsivity on wavelength is as  $R = \eta \cdot \frac{q\lambda}{hc}$ , where  $\eta$  is the quantum efficiency. It can be seen that the responsivity is linearly proportional to

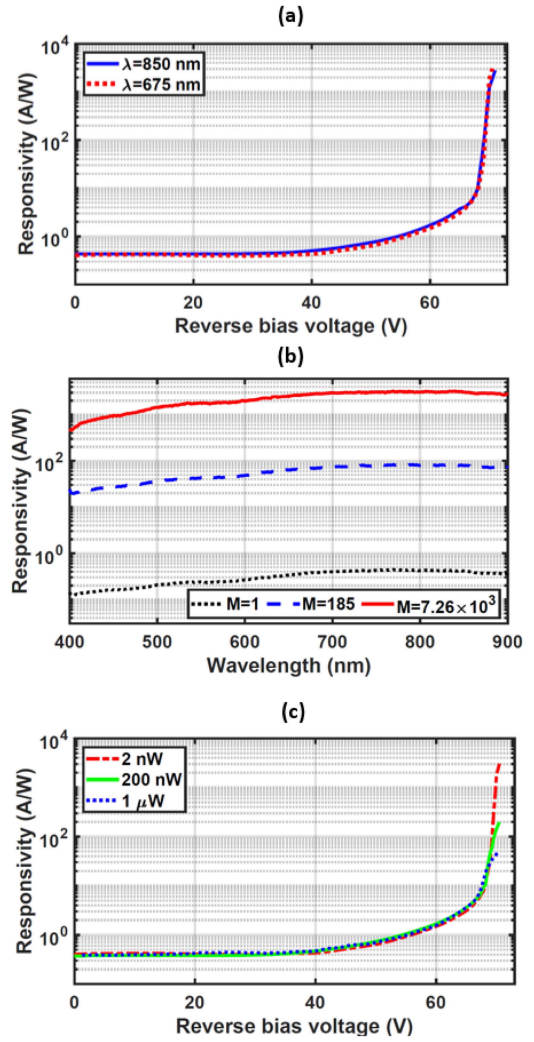


Fig. 6. (a) Responsivity as a function of reverse bias voltage at  $op = 2 \text{ nW}$ . (b) Spectral responsivity at  $op = 2 \text{ nW}$  for different gain  $M$ . (c) Responsivity at  $850 \text{ nm}$  as a function of reverse bias voltage for different optical powers. Measurements are done for the EFLC-APD with  $rw = 0.6 \mu\text{m}$  and  $ra = 19 \mu\text{m}$ .

the wavelength. This is because as the wavelength increases, the energy per photon becomes smaller, but each photon is still able to generate a carrier as long as the photon energy is larger than the bandgap energy. As a result, the responsivity is higher at longer wavelengths. However, at long wavelengths a considerable portion of the transmitted photons is absorbed in a deep depth where the electric field is very weak or non-existent to drive carriers towards the cathode. Therefore, the dominant transfer mechanism shifts from carrier drift to carrier diffusion, giving room to carrier recombination and resulting in a decrease in responsivity. In addition, there is an influence of the optical transmission through the isolation and passivation stack. The spectral responsivity shows an almost flat shape at long wavelengths ( $650 \text{ nm} < \lambda < 900 \text{ nm}$ ) with an unamplified maximum value of  $0.44 \text{ A/W}$  at  $\lambda = 770 \text{ nm}$  at  $M = 1$ . Such high unamplified responsivity at long wavelengths is due to the thick detection zone as expected from the TCAD simulation results. It is shown that a maximum responsivity of  $3.05 \times 10^3 \text{ A/W}$  at the gain of  $7.26 \times 10^3$  is achieved for near-infrared wavelengths.

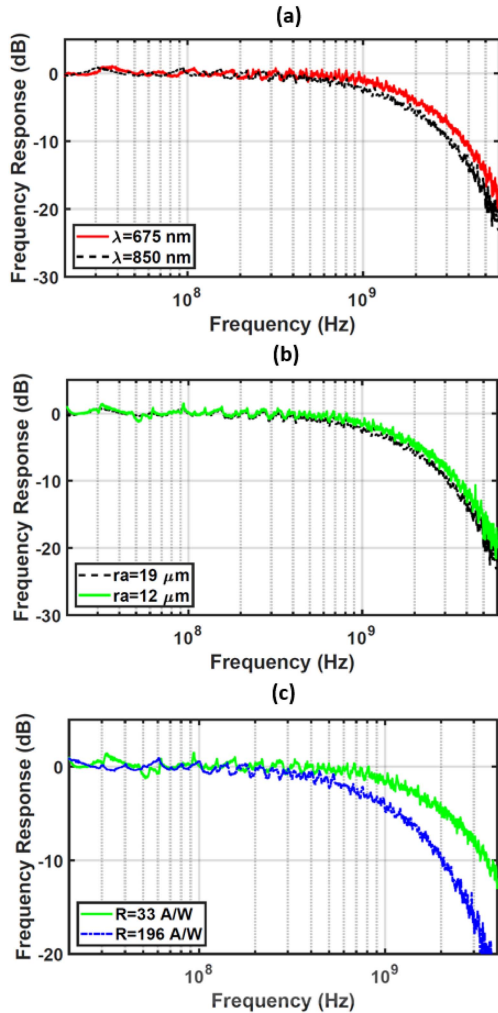


Fig. 7. Normalized frequency responses of (a) EFLC-APD with  $r_w = 0.6 \mu\text{m}$  and  $r_a = 19 \mu\text{m}$  for two wavelengths at  $M = 80$ . (b) EFLC-APD with  $r_w = 0.6 \mu\text{m}$  and two diode sizes of  $r_a = 12 \mu\text{m}$  and  $r_a = 19 \mu\text{m}$  at  $\lambda = 850 \text{ nm}$  and at  $M = 80$ . (c) EFLC-APD with  $r_w = 0.6 \mu\text{m}$  and  $r_a = 12 \mu\text{m}$  at different responsivities at  $\lambda = 850 \text{ nm}$ .

Fig. 6(c) illustrates the dependency of the responsivity on the optical power. At different optical power, the maximum achievable responsivity is different. In fact, the maximum achievable responsivity is lower at higher optical power because of the saturation effect of the multiplication process at high optical powers due to partial screening of the electric field by many charges. Maximum responsivities for 850 nm of 196 and 48 A/W, both corresponding to the operating voltage of 70.5 V, are achieved at the optical powers of 200 nW and 1  $\mu\text{W}$ , respectively.

### C. Frequency Response and Bandwidth

The frequency response of the EFLC-APD ( $r_w = 0.6 \mu\text{m}$ ,  $r_a = 19 \mu\text{m}$ ) was measured for the two wavelengths of 675 nm and 850 nm with an optical power of 200 nW as shown in Fig. 7. Measurements were done using a vector network analyzer (Rohde & Schwarz ZNB8), which received the RF signal through a high voltage bias-tee (Freq  $\sim 5 \text{ MHz} - 18 \text{ GHz}$ ). The maximum bandwidth of 1.6 GHz for  $r_w = 0.6 \mu\text{m}$  and  $r_a = 19 \mu\text{m}$  is

achieved at  $\lambda = 675 \text{ nm}$  and  $V = 69 \text{ V}$ , corresponding to the gain of 80 and responsivity of 32 A/W which demonstrates  $\sim 90\%$  improvement compared to the results reported in Ref [16]. This is because the electric field is distributed across a larger thickness of about  $20 \mu\text{m}$  compared to a thickness of the drift region in [16] of only about  $8 \mu\text{m}$ , which left some contribution of slow carrier diffusion. Therefore, the contribution of slow carrier diffusion in this APD is significantly lowered compared to that of the APD in [16]. Nonetheless, the EFLC-APD uses the concept of separate multiplication and absorption region to achieve high responsivity with the inevitable bandwidth limitation by carrier drift time in a thick absorption zone.

The frequency response measured for the same EFLC-APD at  $\lambda = 850 \text{ nm}$  shows a maximum achievable bandwidth of 1.2 GHz at the same gain ( $M = 80$ ) and responsivity ( $R = 33 \text{ A/W}$ ). This bandwidth is 400 MHz lower compared to that obtained for a wavelength of 675 nm as reported in [30] due to the larger penetration depth of 850 nm light. However, the bandwidth is still 350 MHz larger than reported in [16] for 850 nm. This is due to the fact that more of the photons with longer wavelengths are absorbed deeper and thus the transit time of the photogenerated electrons to reach the cathode is higher.

It should be noticed that the frequency response is determined by the transit time of photogenerated electrons to reach the cathode, which could be reduced by shortening the carrier drift distance and increasing the electric field intensity. Since in this APD, the electrons generated in the peripheral volume are guided towards the multiplication region, and even the electrons generated far away from the cathode contribute to the photocurrent; thus, the frequency response is expected to improve by reducing the size ( $r_a$ ) of the EFLC-APD.

Fig. 7(b) presents the normalized frequency response of the EFLC-APDs with two different sizes ( $r_a = 12 \mu\text{m}$  and  $r_a = 19 \mu\text{m}$ ) at  $\lambda = 850 \text{ nm}$  and  $M = 80$ . It can be observed that by reducing  $r_a$  from  $19 \mu\text{m}$  to  $12 \mu\text{m}$ , the bandwidth increases from 1.2 GHz to 1.5 GHz. This improvement is attributed to the electron drift time reduction due to the shortening of the radial carrier drift distance as well as to the increase in the electric field strength distributed across the detection zone as discussed in Section II. Since the responsivity remains the same for both structures, the APD with  $r_a = 12 \mu\text{m}$  achieves a higher R-BW product. It is worth mentioning that we could enhance the bandwidth by shrinking the EFLC-APD while maintaining its responsivity. An important aspect that should be pointed out is that, due to the high sensitive-area to total-area ratio, it is possible to provide enough active area when it is downsized.

We should note that the bandwidth drops at higher responsivity because of the avalanche build-up time effect. In fact, at the maximum responsivity, we have the highest multiplication factor, and as the avalanche process takes time, the avalanche build-up time is high, which causes a bandwidth decrease. In order to demonstrate this effect, Fig. 7(c) shows the frequency response at the maximum responsivity of 196 A/W corresponding to the gain of 466 at the optical power of 200 nW. It shows that the bandwidth is reduced to 760 MHz. However, for this gain and optical power, the effect of avalanche build-up time is not strongly pronounced (compared to 1.5 GHz bandwidth at a gain

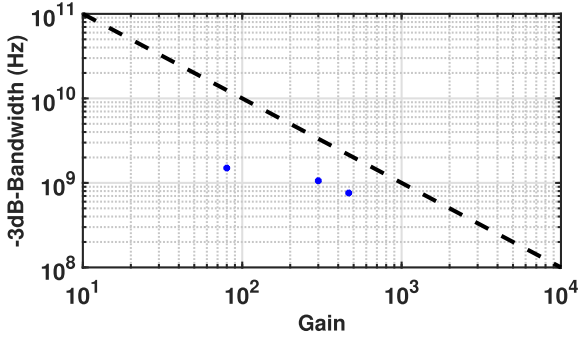


Fig. 8. Bandwidth vs. gain of EFLC-APD with  $r_w = 0.6 \mu\text{m}$  and  $r_a = 12 \mu\text{m}$  at the optical power of 200 nW. The dashed line represents the gain-bandwidth product of 1 THz [32].

of 80, we lose only a factor of about 2 in bandwidth). We expect higher bandwidth reduction at higher gains (at lower optical powers). Accordingly, based on the intended application, the trade-off between bandwidth and sensitivity can be optimized. For instance, in applications that work at low frequencies, one can utilize the maximum responsivity. Fig. 8 shows the bandwidth versus gain at the optical power of 200 nW. Bandwidths of 1.5, 1.06, and 0.76 GHz are obtained for gains of 80, 300, and 466, respectively. It can be seen that the bandwidth decreases with increasing gain. The dashed line in Fig. 8 represents a gain-bandwidth product of 1 THz that shows the gain-bandwidth product limit [32]. The left point (see Fig. 8) at  $M = 80$  and a bandwidth of about 1.5 GHz approaches the bandwidth limit determined by the carrier drift time through the thick absorption zone.

#### D. Noise Characteristic

The signal-to-noise ratio enhancement, achieved by avalanche gain, is actually compromised by a gain dependent noise component. Models like the McIntyre's theory [33] or the dead-space model [34], [35] are well established to predict the APD excess noise factor  $F$  for devices with uniform electric field. However, for EFLC-APDs, these models are not applicable, since the electric field is predominately non-uniform (see Fig. 2a). Hence, in the following section, the noise characteristics of the EFLC-APD is studied experimentally.

The noise characterization method utilized in this study was based on the approach presented by [36]. Essentially the power spectral density (PSD) of the APD's photocurrent, stimulated by a laser source in DC mode, is measured for different avalanche gains ( $M$ ). For this experiment, a 642 nm single-mode laser (Thorlabs, LP642-SF20) was used to exclude the effect of mode noise. Various values of  $M$  were obtained by adjusting the operating voltage while measuring the photocurrent using an electrometer (Keysight B2987A). The APD is reverse-biased by applying a negative voltage to the anode, while the cathode is connected to a transimpedance amplifier (TIA LMH3440,  $R_T = 28 \text{ k}\Omega$  and  $BW = 200 \text{ MHz}$ , both measured). The TIA provides the necessary amplification to the photocurrent noise level to be distinguishable from the spectrum analyzer noise floor (R&S FSP, noise floor  $\approx -155 \text{ dBm/Hz}$  up to 500 MHz).

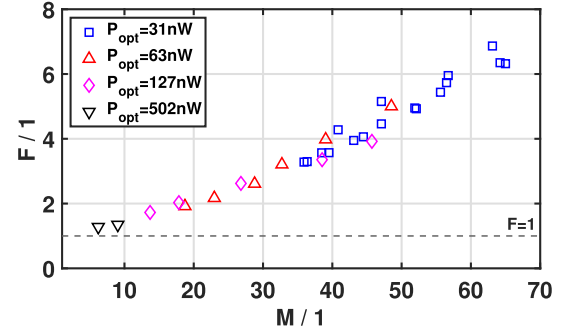


Fig. 9. Measured excess noise factor at  $\lambda = 642 \text{ nm}$ . A relatively narrow dynamic range of the measurement system required a variety of optical power levels to cover a reasonable span of  $M$ .

However, it also poses an additional noise source, that was taken care of by calibration, done in post-processing. For every measured data point of  $M$ , the PSD was acquired (averaged over 5 sweeps from 10 MHz to 100 MHz with 10 kHz resolution bandwidth) with and without light. Their difference equals the PSD of the photocurrent. This calibration method is insufficient, if the photocurrent's PSD is much smaller than the TIA PSD, hence the system sensitivity was defined so that the APD noise has to be equal to the noise of the measurement system. The mean PSD of the TIA with connected APD, biased at  $-1 \text{ V}$ , without light, was  $\approx -127 \text{ dBm/Hz}$  (generally a higher diode capacitance elevates the TIA noise spectrum, however for the presented APD the capacitance at smallest bias voltage is already dominated by the PCB parasitics, so the TIA PSD was effectively constant for all bias states up to a saturation limit, which is explained further below). A measurement run started by positioning the fiber (mode field diameter  $\approx 5 \mu\text{m}$ ) above the center of the APD surface. In fact, the fiber was adjusted to the position of maximum photocurrent. The photocurrent is measured at  $M = 1$  ( $V_r = -1 \text{ V}$ ), which gives the reference value for the calculation of  $M$ . After that, the bias voltage is set to a starting value (determined by the system sensitivity and the optical power) and then increased in small steps. For every voltage point, the photocurrent  $I_{APD}$  (i.e.,  $M$ ) and the PSD is measured. At the end of each run another photocurrent measurement at  $M = 1$  is done to ensure that the fiber is still properly positioned. Referring to [36], the excess noise factor  $F$  can be calculated for every data point by

$$F = \frac{\overline{PSD}_{cal} R_{term}}{2qMI_{APD}R_T^2}, \quad (2)$$

where  $q$  is the electron charge,  $R_{term}$  is the input resistance of the spectrum analyzer ( $50 \Omega$ ) and  $\overline{PSD}_{cal}$  is the mean value of the calibrated PSD in the interval from 10 MHz to 100 MHz.

The result of the excess noise measurement is illustrated in Fig. 9. A variety of optical power levels was necessary to cover a reasonable span of  $M$  while respecting the dynamic range of the measurement system. Multiplied photocurrent levels had to be in the range of  $\approx 0.4$  to  $1 \mu\text{A}$ , in order to be utilizable. The measured points within the dynamic range resulted in excess noise factors of 2, 4 and 6 at gains of 17.8, 39, and 56.7, respectively. It is important to mention that due to the non-uniform electric

TABLE I  
PERFORMANCE COMPARISON OF LINEAR-MODE APDS (RT-APD: REACH-THROUGH APD; CA-APD: CURRENT ASSISTED APD)

Parameters	Ref [16]	Ref [38]	Ref [19]	Ref [25]	Ref [13]	Ref [30]	This work	This work
Technology	0.35 $\mu\text{m}$	0.25 $\mu\text{m}$	0.35 $\mu\text{m}$	0.35 $\mu\text{m}$	45 nm	0.18 $\mu\text{m}$	0.18 $\mu\text{m}$	0.18 $\mu\text{m}$
Structure	n <sup>+</sup> /p-well RT-APD	p <sup>+</sup> /n-well APD	n <sup>+</sup> /p-well RT-APD	p <sup>+</sup> /n-well CA-APD	Double p-well/ deep n-well APD	n <sup>+</sup> /n-well EFLC-APD	n <sup>+</sup> /n-well EFLC-APD	n <sup>+</sup> /n-well EFLC-APD
Active area	r=30 $\mu\text{m}$	10×10 $\mu\text{m}^2$	r=30 $\mu\text{m}$	40×40 $\mu\text{m}^2$	20×20 $\mu\text{m}^2$	r=19 $\mu\text{m}$	r=12 $\mu\text{m}$	r=19 $\mu\text{m}$
Operating voltage	63 V	12.2 V	115 V	68 V	20.8 V	69 V	60 V	69 V
Optical power	500 nW	1 mW	2 $\mu\text{W}$	2 $\mu\text{W}$	100 $\mu\text{W}$	200 nW	200 nW	200 nW
Wavelength	670 nm	850 nm	670 nm	830 nm	850 nm	675 nm	850 nm	850 nm
Gain	50	16.7	50	43.9	23	80	80	80
Responsivity	20.5 A/W	0.2 A/W	20.5 A/W	13.17 A/W	0.56 A/W	33 A/W	33 A/W	33 A/W
Bandwidth	850 MHz	5.6 GHz	1.25 GHz	275 MHz	8.4 GHz	1.6 GHz	1.5 GHz	1.2 GHz
R-BW product	17.4 $\frac{\text{A}}{\text{W}} \cdot \text{GHz}$	1.1 $\frac{\text{A}}{\text{W}} \cdot \text{GHz}$	25.6 $\frac{\text{A}}{\text{W}} \cdot \text{GHz}$	3.6 $\frac{\text{A}}{\text{W}} \cdot \text{GHz}$	4.7 $\frac{\text{A}}{\text{W}} \cdot \text{GHz}$	52.8 $\frac{\text{A}}{\text{W}} \cdot \text{GHz}$	49.5 $\frac{\text{A}}{\text{W}} \cdot \text{GHz}$	39.6 $\frac{\text{A}}{\text{W}} \cdot \text{GHz}$

field, present in the EFLC-APD structure, neither McIntyre's theory [33] nor the dead-space model [34], [35] can be utilized to account for the excessive noise observed in these diodes. These models are derived for structures with uniform electric fields. Nevertheless, due to a wavelength dependence of the dead-space effect [37], higher excess noise has to be expected for increased wavelength.

## V. COMPARISON

The excess noise factors obtained are comparable to those [36] of the planar n<sup>+</sup>/p-well APD in 0.35  $\mu\text{m}$  high-voltage (HV) CMOS with a uniform electric field [16]. F of this 0.35  $\mu\text{m}$  HV APD was 6 at M = 50 and about 6.5 at M = 60. When we compare the thickness of the multiplication region (where  $E \gtrsim 2 \times 10^5$  V/cm), it is 0.73  $\mu\text{m}$  in the 0.35  $\mu\text{m}$  HV APD and about 0.9  $\mu\text{m}$  in the EFLC 0.18  $\mu\text{m}$  HV APD (both for M = 60). A thicker multiplication region is generally better for a lower excess noise. But the crowding of the multiplied carriers towards lower radius (like the crowding of the field lines when they approach to the inner end of the multiplication region) obviously counteracts this advantage of the thicker multiplication region.

To better highlight the contribution of this work over the state-of-the-art, Table 1 shows a comparison of the key performance parameters of the EFLC-APD with various silicon photodetectors fabricated in standard CMOS technologies. It should be noted that the achieved maximum bandwidth of 1.5 GHz shows 77% and 550% improvement compared to results reported in Ref. [16] and [25] for wavelengths of 670 and 830 nm, respectively. This APD additionally shows a responsivity improvement of 60% and 240% compared to results reported in Ref. [16] and [25] respectively. Furthermore, the presented EFLC-APD achieves a responsivity-bandwidth product of 49.5  $\frac{\text{A}}{\text{W}} \cdot \text{GHz}$ , corresponding to the responsivity and bandwidth of R = 33 A/W and BW = 1.5 GHz, respectively, which shows a significant improvement compared to the literature according to Table I.

## VI. CONCLUSION

A characterization of the electric field-line crowding-based avalanche photodiode is presented. It is shown that a hemispherical electric field distribution formed across the entire volume of the EFLC-APD leads to a thick hemispherical detection zone in which the electrons generated in the entire volume are accelerated towards the cathode. The EFLC-APD achieves a maximum responsivity of  $3.05 \times 10^3$  A/W in the red and near-infrared spectral range due to its thick absorption region. Furthermore, because of the high electric field distributed over the structure, it provides a maximum bandwidth of 1.5 GHz at  $\lambda = 850$  nm, that is an improvement of 77% and 550% compared to results reported in Ref. [16] and [25], respectively. In addition, the EFLC-APD shows the responsivity-bandwidth product of 49.5  $\frac{\text{A}}{\text{W}} \cdot \text{GHz}$ , which represents a significant improvement over the state-of-the-art. Also the excess noise was investigated, F=6 was measured at a gain of 56.7. Especially for range-finding sensors, which use near-infrared light, this APD should be well appropriate.

## ACKNOWLEDGMENT

The authors would like to thank A. Zimmer from XFAB for technical support as well as D. Sommer for fabrication support.

## REFERENCES

- [1] M. M. Hossain et al., "Low-noise speed-optimized large area CMOS avalanche photodetector for visible light communication," *J. Lightw. Technol.*, vol. 35, no. 11, pp. 2315–2324, Jun. 2017.
- [2] E. Kamrani, F. Lesage, and M. Sawan, "Low-noise, high-gain transimpedance amplifier integrated with SiAPD for low-intensity near-infrared light detection," *IEEE Sensors J.*, vol. 14, no. 1, pp. 258–269, Jan. 2014.
- [3] L. Zhang et al., "A comparison of APD-and SPAD-based receivers for visible light communications," *J. Lightw. Technol.*, vol. 36, no. 12, pp. 2435–2442, Jun. 2018.
- [4] P. Brandl, T. Jukić, R. Enne, K. Schneider-Hornstein, and H. Zimmermann, "Optical wireless APD receiver with high background-light immunity for increased communication distances," *IEEE J. Solid-State Circuits*, vol. 51, no. 7, pp. 1663–1673, Jul. 2016.



- [5] H.-S. Cho, C.-H. Kim, and S.-G. Lee, "A high-sensitivity and low-walk error LADAR receiver for military application," *IEEE Trans. Circuits Syst. I: Regular Papers*, vol. 61, no. 10, pp. 3007–3015, Oct. 2014.
- [6] H.-Z. Song, "Avalanche photodiode focal plane arrays and their application to laser detection and ranging," in *Advances in Photodetectors-Research and Applications*. London, U.K.: IntechOpen, 2018, pp. 145–168.
- [7] O. Shcherbakova, L. Pancheri, G.-F. Dalla Betta, N. Massari, and D. Stoppa, "3D camera based on linear-mode gain-modulated avalanche photodiodes," in *Proc. IEEE Int. Solid-State Circuits Conf. Dig. Tech. Papers*, 2013, pp. 490–491.
- [8] Y. Dong et al., "Germanium-tin on silicon avalanche photodiode for short-wave infrared imaging," in *Proc. Symp. VLSI Technol. (VLSI- Technol.): Dig. Tech. Papers*. IEEE, 2014, pp. 1–2.
- [9] K. Iiyama, H. Takamatsu, and T. Maruyama, "Hole-injection-type and electron-injection-type silicon avalanche photodiodes fabricated by standard 0.18  $\mu\text{m}$  CMOS process," *IEEE Photon. Technol. Lett.*, vol. 22, no. 12, pp. 932–934, Jun. 2010.
- [10] F.-P. Chou, C.-W. Wang, Z.-Y. Li, Y.-C. Hsieh, and Y.-M. Hsin, "Effect of deep N-Well bias in an 850-nm Si photodiode fabricated using the CMOS process," *IEEE Photon. Technol. Lett.*, vol. 25, no. 7, pp. 659–662, Apr. 2013.
- [11] S. Nayak, A. H. Ahmed, A. Sharkia, A. S. Ramani, S. Mirabbasi, and S. Shekhar, "A 10-Gb/s- 18.8 dBm sensitivity 5.7 mW fully-integrated optoelectronic receiver with avalanche photodetector in 0.13  $\mu\text{m}$  CMOS," *IEEE Trans. Circuits Syst. I: Regular Papers*, vol. 66, no. 8, pp. 3162–3173, Aug. 2019.
- [12] M.-J. Lee and W.-Y. Choi, "A silicon avalanche photodetector fabricated with standard CMOS technology with over 1 THz gain-bandwidth product," *Opt. Exp.*, vol. 18, no. 23, pp. 24189–24194, 2010.
- [13] W. Zhi, Q. Quan, P. Yu, and Y. Jiang, "A 45 nm CMOS avalanche photodiode with 8.4 GHz bandwidth," *Micromachines*, vol. 11, no. 1, 2020, Art. no. 65.
- [14] M.-J. Lee, "First CMOS silicon avalanche photodetectors with over 10-GHz bandwidth," *IEEE Photon. Technol. Lett.*, vol. 28, no. 3, pp. 276–279, Feb. 2016.
- [15] Y. S. Kim, I. S. Jun, and K. H. Kim, "Design and characterization of CMOS avalanche photodiode with charge sensitive preamplifier," *IEEE Trans. Nucl. Sci.*, vol. 55, no. 3, pp. 1376–1380, Jun. 2008.
- [16] B. Steindl, R. Enne, S. Schidl, and H. Zimmermann, "Linear mode avalanche photodiode with high responsivity integrated in high-voltage CMOS," *IEEE Electron Device Lett.*, vol. 35, no. 9, pp. 897–899, Sep. 2014.
- [17] B. Steindl, W. Gaberl, R. Enne, S. Schidl, K. Schneider-Hornstein, and H. Zimmermann, "Linear mode avalanche photodiode with 1-GHz bandwidth fabricated in 0.35- $\mu\text{m}$  CMOS," *IEEE Photon. Technol. Lett.*, vol. 26, no. 15, pp. 1511–1514, Aug. 2014.
- [18] Z. Cheng, H. Xu, and Y. Chen, "Design of low noise avalanche photodiode single element detectors and linear arrays through CMOS process," *Proc. SPIE*, vol. 10978, pp. 70–77, 2019.
- [19] R. Enne, B. Steindl, and H. Zimmermann, "Speed optimized linear-mode high-voltage CMOS avalanche photodiodes with high responsivity," *Opt. Lett.*, vol. 40, no. 19, pp. 4400–4403, 2015.
- [20] M.-J. Lee, H. Rucker, and W.-Y. Choi, "Effects of guard-ring structures on the performance of silicon avalanche photodetectors fabricated with standard CMOS technology," *IEEE Electron Device Lett.*, vol. 33, no. 1, pp. 80–82, Jan. 2012.
- [21] W. Wang, H.-A. Zeng, F. Wang, G. Wang, Y. Xie, and S. Feng, "A speed-optimized, low-noise APD with 0.18  $\mu\text{m}$  CMOS technology for the VLC applications," *Modern Phys. Lett. B*, vol. 34, no. 29, 2020, Art. no. 2050321.
- [22] T. Wang et al., "Effects of guard-ring's depth and space on the performance of silicon avalanche photodetector arrays with TCAD simulation," *Proc. SPIE*, vol. 12065, pp. 602–607, 2021.
- [23] D. Shin, B. Park, Y. Chae, and I. Yun, "The effect of a deep virtual guard ring on the device characteristics of silicon single photon avalanche diodes," *IEEE Trans. Electron Devices*, vol. 66, no. 7, pp. 2986–2991, Jul. 2019.
- [24] S. S. K. Poushi, H. Mahmoudi, M. Hofbauer, B. Steindl, K. Schneider-Hornstein, and H. Zimmermann, "Experimental and simulation study of fill-factor enhancement using a virtual guard ring in n/p-well CMOS single-photon avalanche diodes," *Proc. SPIE*, vol. 60, 2021, Art. no. 067105.
- [25] G. Jegannathan, H. Ingelberts, S. Boulanger, and M. Kuijk, "Current assisted avalanche photo diodes (CAAPDs) with separate absorption and multiplication region in conventional CMOS," *Appl. Phys. Lett.*, vol. 115, no. 13, 2019, Art. no. 132101.
- [26] E. Van Sieleghem et al., "A near-infrared enhanced silicon single-photon avalanche diode with a spherically uniform electric field peak," *IEEE Electron Device Lett.*, vol. 42, no. 6, pp. 879–882, Jun. 2021.
- [27] E. Van Sieleghem et al., "A backside-illuminated charge-focusing silicon SPAD with enhanced near-infrared sensitivity," *IEEE Trans. Electron Devices*, vol. 69, no. 3, pp. 1129–1136, Mar. 2022.
- [28] K. Morimoto et al., "3.2 megapixel 3D-stacked charge focusing SPAD for low-light imaging and depth sensing," in *Proc. IEEE Int. Electron Devices Meeting*, 2021, pp. 20–2.
- [29] E. Engelmann, W. Schmailzl, P. Iskra, F. Wiest, E. Popova, and S. Vinogradov, "Tip avalanche photodiode—A new generation silicon photomultiplier based on non-planar technology," *IEEE Sensors J.*, vol. 21, no. 5, pp. 6024–6034, Mar. 2021.
- [30] S. K. Poushi, B. Goll, K. Schneider-Hornstein, M. Hofbauer, and H. Zimmermann, "CMOS integrated 32 A/W and 1.6 GHz avalanche photodiode based on electric field-line crowding," *IEEE Photon. Technol. Lett.*, vol. 34, no. 18, pp. 945–948, Sep. 2022.
- [31] "Silvaco atlas user's manual." Accessed: 2022. [Online]. Available: <https://www.silvaco.com>
- [32] D. Decoster and J. Harari, *Optoelectronic Sensors*. Hoboken, NJ, USA: Wiley, 2013.
- [33] R. J. McIntyre, "Multiplication noise in uniform avalanche diodes," *IEEE Trans. Electron Devices*, vol. ED-13, no. 1, pp. 164–168, Jan. 1966.
- [34] B. E. A. Saleh, M. M. Hayat, and M. C. Teich, "Effect of dead space on the excess noise factor and time response of avalanche photodiodes," *IEEE Trans. Electron Devices*, vol. 37, no. 9, pp. 1976–1984, Sep. 1990.
- [35] M. M. Hossain et al., "Low-noise speed-optimized large area CMOS avalanche photodetector for visible light communication," *J. Lightw. Technol.*, vol. 35, no. 11, pp. 2315–2324, Jun. 2017.
- [36] T. Jukić, P. Brandl, and H. Zimmermann, "Determination of the excess noise of avalanche photodiodes integrated in 0.35- $\mu\text{m}$  CMOS technologies," *Proc. SPIE*, vol. 57, no. 4, 2018, Art. no. 044101.
- [37] A. R. Pauchard, P.-A. Besse, and R. S. Popovic, "Dead space effect on the wavelengthdependence of gain and noise in avalanche photodiodes," *IEEE Trans. Electron Devices*, vol. 47, no. 9, pp. 1685–1693, Sep. 2000.
- [38] M.-J. Lee, J.-M. Lee, H. Rucker, and W.-Y. Choi, "Bandwidth improvement of CMOS-APD with carrier-acceleration technique," *IEEE Photon. Technol. Lett.*, vol. 27, no. 13, pp. 1387–1390, Jul. 2015.